RSC Advances

PAPER

View Article Online
View Journal | View Issue

Open Access Article. Published on 10 November 2021. Downloaded on 12/4/2025 4:48:14 PM.
This article is licensed under a Creative Commons Attribution-NonCommercial 3.0 Unported Licence.

Check for updates

Cite this: *RSC Adv.*, 2021, **11**, 36148

Structural, morphological, Raman, dielectric and electrical properties of $La_{1-2x}Ba_xBi_xFeO_3$ ($0.00 \leq x \leq 0.20$) compounds

E. M. Benali,[ab]* A. Benali,[abc] M. Bejar,[a] E. Dhahri,[a] M. P. F. Graca,[c] M. A. Valente[c] and B. F. O. Costa[b]

Received 9th July 2021
Accepted 1st November 2021

DOI: 10.1039/d1ra05299c

rsc.li/rsc-advances

$La_{1-2x}Ba_xBi_xFeO_3$ ($0.00 \leq x \leq 0.20$) nanoparticles were prepared by the auto-combustion method using glycine as a combustion fuel. X-ray diffractometry (XRD) measurements confirmed the orthorhombic structure of the synthesized compounds with the *Pnma* space group as a principal majority phase and showed the presence of a very minor secondary phase when $x > 0.1$. The nanosize criterion of the prepared compounds was confirmed from the crystallite size values calculated using the Williamson–Hall formalism. The relaxation process has been studied by the frequency dependence of the imaginary parts of impedance and modulus (Z'' and M'') which satisfied the Arrhenius law. Nyquist plots allowed us to obtain an adequate equivalent circuit involving the grains and grain boundary contributions. The activation energies calculated from Z'', M'' and the resistance of both contributions deduced from the Nyquist plots are found to be very similar. The conduction mechanism has been analyzed using the temperature dependence of the exponent Jonscher's power law parameter which confirms the NSPT conduction mechanism type for all compounds with an enhancement of the binding energy of the charge carrier (W_H) with the substitution.

1 .Introduction

Lanthanum ferrite ($LaFeO_3$) perovskite structures with the general formula ABO_3 are considered as promising materials due to their interesting physico-chemical properties which make them potential candidates for a wide range of application areas.[1–4] These physico-chemical properties depend not only on the composition but also on various parameters, such as the porosity and the particle size which are directly related to the synthesis method. Accordingly, pure and doped lanthanum ferrites have been prepared by several preparation processes such as microwave,[5] hydrothermal,[6] polymer pyrolysis,[7] sono-chemical methods,[8] sol–gel methods,[9–11] the solid-state route,[12] sonoelectro-chemical synthesis methods[13] and the chemical spin coating method.[14]

Several studies have been focused on the dielectric and electrical properties of the Lanthanum ferrite. In this context, C. Chen *et al.*[15] displayed that the $LaFeO_3$ material exhibits a Debye relaxation with the activation energy of 0.237 eV. Besides, Mizusaki *et al.*[16] reported that this compound presents an oxygen excess structure and p-type conductivity.

On the other side, previous researcher works have shown that the substitution of the La-site with divalent metals and/or Fe-site with transition metals has an important impact on the structural, magnetic, dielectric, electrical and gas sensing properties.[17–19] For instance, it has been confirmed that the "Sr" ions substituted at the A-site of the $LaFeO_3$ compound increase its electrical conductivity.[20] Moreover, E. Cao *et al.*[21] confirmed that the "Na" substitution in the La-site of $LaFeO_3$ enhances

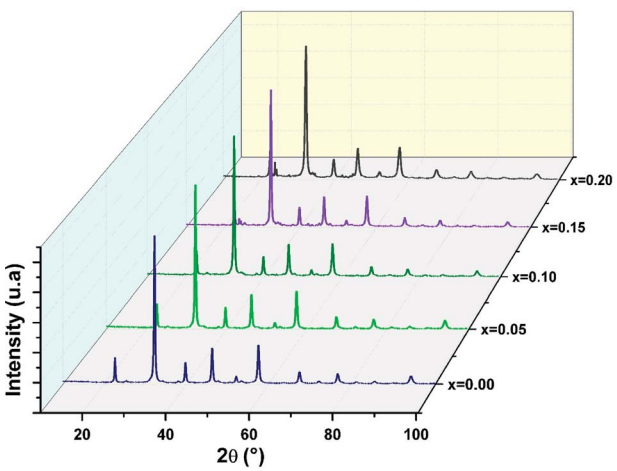

Fig. 1 Comparison of XRD patterns of the $La_{1-2x}Bi_xBa_xFeO_3$ ($x = 0.00$, 0.05, 0.10, 0.15 and 0.20) compounds.

[a]*Laboratoire de Physique Appliquée, Faculté des Sciences, Université de Sfax, B.P. 1171, 3000 Sfax, Tunisie. E-mail: benaliemna93@gmail.com*

[b]*University of Coimbra, CFisUC, Physics Department, Rua Larga, P-3004-516 Coimbra, Portugal*

[c]*I3N and Physics Department, University of Aveiro, 3810-193, Aveiro, Portugal*

© 2021 The Author(s). Published by the Royal Society of Chemistry

Open Access Article. Published on 10 November 2021. Downloaded on 12/4/2025 4:48:14 PM.
This article is licensed under a Creative Commons Attribution-NonCommercial 3.0 Unported Licence.

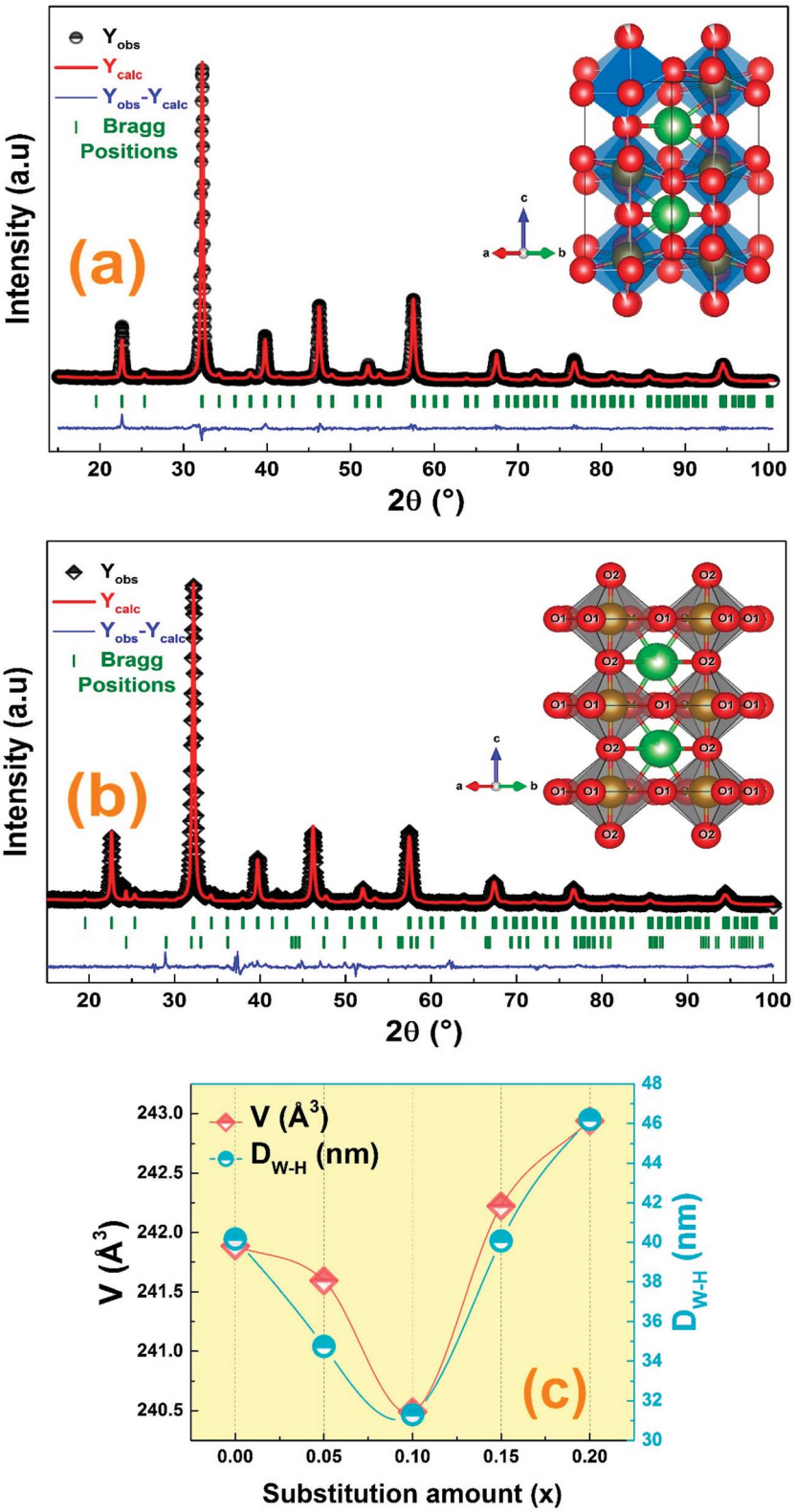

Fig. 2 The structural refined XRD patterns of the (a) $LaFeO_3$ ($x = 0.0$) and (b) $La_{1-2x}Bi_xBa_xFeO_3$ ($x = 0.15$) compounds with the crystal structure. (c) The variation of cell volume and $D_{W\text{-}H}$ crystallite size with substitution concentration.

Open Access Article. Published on 10 November 2021. Downloaded on 12/4/2025 4:48:14 PM.
This article is licensed under a Creative Commons Attribution-NonCommercial 3.0 Unported Licence.

this dielectric constant. Another study reported that the Ba substitution at the A-site reduces the electrical resistance.[22] In addition, some studies reported that the substitution of La^{3+} ions by the Bi^{3+} ones leads to an improvement of the conductivity and the electrochemical performance.[23,24]

Moreover, we have previously studied the effect of substituting 20% of La ions by Ba and Bi-ones (10% for each ion), and we confirmed a decrease in electrical resistance and particle size as compared to literature which allowed the use of such material for gas sensing applications.[25]

It is important to mention that we early studied the substitution effect of La^{3+} ions by both Ba^{2+} and Bi^{3+} ones on structural, morphological, and ethanol and H_2S gas sensing. The compound with $x = 0.10$ presents the lowest particle size with highest response to both gases.[26] It was well confirmed that the gas sensing properties of semiconductor materials are highly dependent on both particle size and resistance properties. In the present work we highlighted the substitution effects on conduction mechanism, dielectric relaxation, and electrical properties.

$La_{1-2x}Ba_xBi_xFeO_3$ (x = 0.00, 0.05, 0.10, 0.15, and 0.20) compounds were synthesized by the auto-combustion method where an adequate glycine amount was used as combustible agent.

2. Experimental details

2.1. Characterization tools

The X-ray diffraction (XRD) of the samples was done at room temperature using a Siemens D5000 Diffractometer with Cu-Kα (λ = 0.154184 nm) radiation source and the data were collected in the range of $2\theta = 10°–100°$. Raman spectroscopy was recorded under the backscattering configuration using a Jobin Yvon HR800 system with 520 nm laser excitation source. The morphology of the powder was examined by a TESCAN VEGA3 SBH scanning electron microscope (SEM) equipped with an EDS detector Bruker XFlagh 410 M for elemental composition and the homogeneity of the compounds. For the electrical measurements, two conducting silver layers were coated on both sides of the pellets. Then, the transport properties of the studied materials were measured using an Agilent 4294A in the frequency range 80 Hz–1 MHz and the temperature range 150 K–400 K.

2.2. Materials synthesis

$La_{1-2x}Ba_xBi_xFeO_3$ (x = 0.00, 0.05, 0.10, 0.15 and 0.20) compounds were synthesized by the auto-combustion method described in our previous study.[25]

Stoichiometric amount of high-purity (≥ 99.9%) of iron nitrate $Fe(NO_3)_3 \cdot 9H_2O$, lanthanum nitrate $La(NO_3)_3 \cdot 6H_2O$, barium nitrate $Ba(NO_3)_2$ and bismuth nitrate $Bi(NO_3)_3 \cdot 5H_2O$ are firstly dissolved in distilled water and an appropriate amount of glycine as fuel agent ($C_2H_5NO_2$) was added to the solution and heated at 70 °C with a continuous stirring until getting dark brown viscos gel. The gel was then heated at 170 °C until it automatically ignited and burnt in some few seconds (with very glowing flints) yielding black ashes (fine powder). The obtained powders are sintered at 700 °C for 30 min to obtain the required samples.

2.3. Methodology and calculations equations

(a) Structural properties. The equation of the Williamson Hall's method:[27]

$$\beta \cos(\theta) = \frac{K \times \lambda}{D_{W-H}} + 4\varepsilon \times \sin(\theta) \quad (1)$$

where D_{W-H} is the average crystallite size, λ (1.5405 Å) represents the used wavelength, θ is the Bragg angle of the most intense peak, β is the full-width at half maximum (FWHM), K is the shape factor and ε is the effective strain.

(b) Raman scattering spectra. The orthorhombic structure and *Pnma* space group present 24 active Raman modes given by the following equation:[28]

$$\Gamma = 7A_g + 7B_{1g} + 5B_{2g} + 5B_{3g} \quad (2)$$

(c) Complex impedance spectra. The Arrhenius equation described as follow:

$$\mathrm{Ln}(f_{max}) = \ln(f_0) + \left[\left(-\frac{E_a}{k_B}\right) \times \frac{1}{T}\right] \quad (3)$$

the Arrhenius power law used for the variation of $\ln(R_{jg,\ g})$ *vs.* $1000/T$:

$$R = R_0 \exp\left(\frac{E_a}{k_B \times T}\right) \quad (4)$$

(d) Complex electrical modulus analysis. The Bergman proposed Kohlrausch, Williams and Watts (KWW) expression described as bellow:[29]

$$M'' = \frac{M''_{max}}{(1-\beta) + \frac{\beta}{1+\beta}\left[\beta\left(\frac{\omega_{max}}{\omega}\right) + \left(\frac{\omega}{\omega_{max}}\right)^{\beta}\right]} \quad (5)$$

where M''_{max} is the maximum value of the imaginary part of modulus M'', ω_{max} is the maximum angular frequency, β is

Table 1 Crystallite size (D_{W-H}) and grain size (D_{SEM}) values of $La_{1-2x}Ba_xBi_xFeO_3$ (x = 0.00, 0.05, 0.10, 0.15 and 0.20) compounds

	0.00	0.05	0.10	0.15	0.20
a (Å)	5.548	5.545	5.5401	5.553	5.559
b (Å)	7.848	7.846	7.820	7.831	7.832
c (Å)	5.555	5.553	5.551	5.5702	5.579
V (Å^3)	241.886	241.593	240.489	242.223	242.938
χ^2	2.049	2.214	2.756	2.932	2.660
Fe–O_1 (Å)	1.962	1.970	1.862	1.971	1.962
Fe–O_2 (Å)	2.106	2.396	2.385	2.259	2.157
Fe–O_1–Fe (°)	150.961	139.514	137.853	136.588	138.701
Fe–O_2–Fe (°)	174.517	169.263	177.243	178.274	178.357
D_{W-H} (nm)	40.170	34.749	31.298	40.072	46.200
D_{SEM} (μm)	0.769	0.704	0.628	0.893	0.967

 © 2021 The Author(s). Published by the Royal Society of Chemistry

Open Access Article. Published on 10 November 2021. Downloaded on 12/4/2025 4:48:14 PM.
This article is licensed under a Creative Commons Attribution-NonCommercial 3.0 Unported Licence.

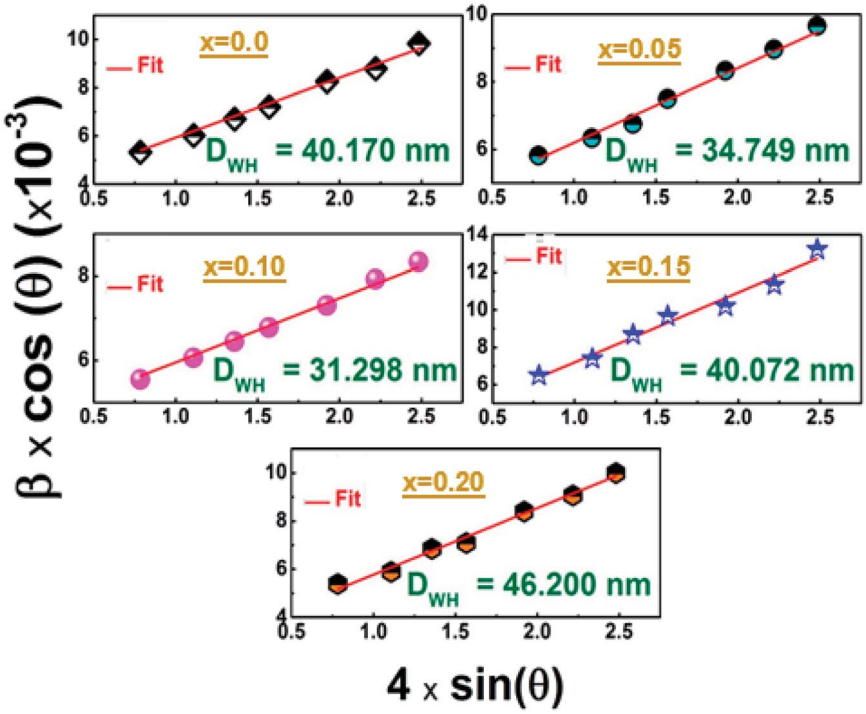

Fig. 3 Williamson–Hall plots of the of the $La_{1-2x}Bi_xBa_xFeO_3$ (x = 0.0, 0.05, 0.1, 0.15 and 0.2) compounds.

a stretching parameter ($0 < \beta < 1$) which indicates the deviation from the Debye relaxation ($\beta = 1$).[30]

(e) The electrical conductivity. The Arrhenius' law related to the conductivity is given by the following expression:[31]

$$\sigma_{ac} \times T = \sigma_0 \exp\left(-\frac{E_a}{k_B \times T}\right) \quad (6)$$

The Jonscher's power law used to adjust the conductivity:[32]

$$\sigma = \sigma_{dc} + A\omega^s \quad (7)$$

where σ_{dc}: is the direct current conductivity, A and s are the pre-exponential and the exponent factors, respectively.

According to the NSPT model, the exponent s is given by the following equation:[33]

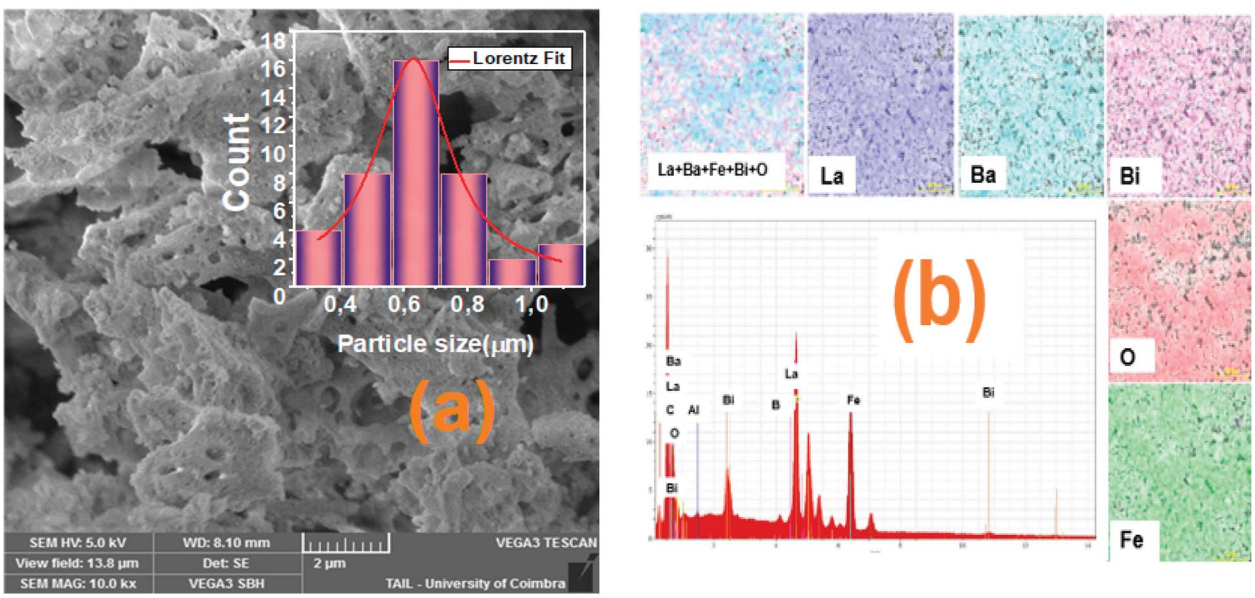

Fig. 4 (a) SEM image and histogram plot for particle size distribution of sample with x = 0.10 and (b) the EDS spectrum with the mapping of chemical elements.

Open Access Article. Published on 10 November 2021. Downloaded on 12/4/2025 4:48:14 PM.
This article is licensed under a Creative Commons Attribution-NonCommercial 3.0 Unported Licence.

Table 2 Atomic weight $(\%)_{EDS}$ of $La_{1-2x}Ba_xBi_xFeO_3$ (x = 0.00, 0.05, 0.10, 0.15 and 0.20) compounds

x	La $(\%)_{EDS}$	Fe $(\%)_{EDS}$	O $(\%)_{EDS}$	Bi $(\%)_{EDS}$	Ba $(\%)_{EDS}$
0.00	17.96	17.31	56.23	—	—
0.05	18.37	20.15	61.26	0.95	1.02
0.10	14.62	17.70	54.82	1.78	1.83
0.15	14.22	19.31	60.96	3.02	3.04
0.20	11.89	19.27	59.48	3.89	3.95

$$s = 1 + \frac{4}{\frac{W_H}{k_B T} - \ln(\omega\tau_0)} \quad (8)$$

where W_H is the bonding energy of the charge carrier in its localized sites and τ_0: is the relaxation time of the material.

$$s = 1 + \frac{4k_B T}{W_H} \quad (9)$$

3. Results and discussion

3.1 Structural properties

Fig. 1 denotes the X-ray room temperature diffraction patterns of the prepared $La_{1-2x}Ba_xBi_xFeO_3$ (x = 0.00, 0.05, 0.10, 0.15 and 0.20) compounds. As shown in this figure, the XRD patterns of all prepared compounds present the same diffraction peaks of the $LaFeO_3$ compound[34] which confirms that they crystallized in an orthorhombic structure with *Pnma* space group. Moreover, some additional diffraction peaks have been detected for compounds with a high amount of Bi^{3+} and Ba^{2+} ions (>10%). Using the X'pert-High score software, these minoritarian secondary phases have been identified to be the "$Bi_2O_{2.7}$" and "$BaFeLaO_4$" phases. To better understand the effect of simultaneous substitution of La^{3+} ions by Bi^{3+} and Ba^{2+} ones on structural parameters, we performed the adjustment of the XRD patterns of all compounds according to the Rietveld method[35] using the Fullprof software[36]. The Rietveld refinement results for all compounds are presented in Fig. 2 and the resulting cell parameters and volume are regrouped in Table 1. As the goodness of refinement is evaluated by the χ^2 values (Table 1), which were found to be of low values confirming the high quality of refinement for all compounds.

From the detailed structural analysis, the Rietveld refinement parameters of Ba and Bi doped $LaFeO_3$ nanoparticles are carried out by assuming the orthorhombic structure with the *Pnma* space group. The parameters obtained from the structural refinement of the X-ray patterns are collected in Table 1. The ionic positions allow us to draw the graphical model of our prepared sample Fig. 2(c).

From Table 1, we can notice that the insertion of Ba and Bi ions in the A-site leads to a variation of all the obtained structural parameters. Also, we observe a variation of the Fe–O–Fe angle and the Fe–O distance, which can be explained by the difference in the size of the cations in the A-site, since the ions radius of Ba^{2+} (1.42 Å) and Bi^{3+} (1.17 Å) are larger than that of La^{3+} (1.16 Å) one.[37] Normally, the increase of substitution amount should be accompanied by an increase in the cell parameters and cell volume which is not the case. All the structural parameters are found to decrease with the substitution amount to reach minimum values for $x = 0.1$ sample and increase for further substitution. In fact, this behavior has been studied in previous work, and has been found to be related to

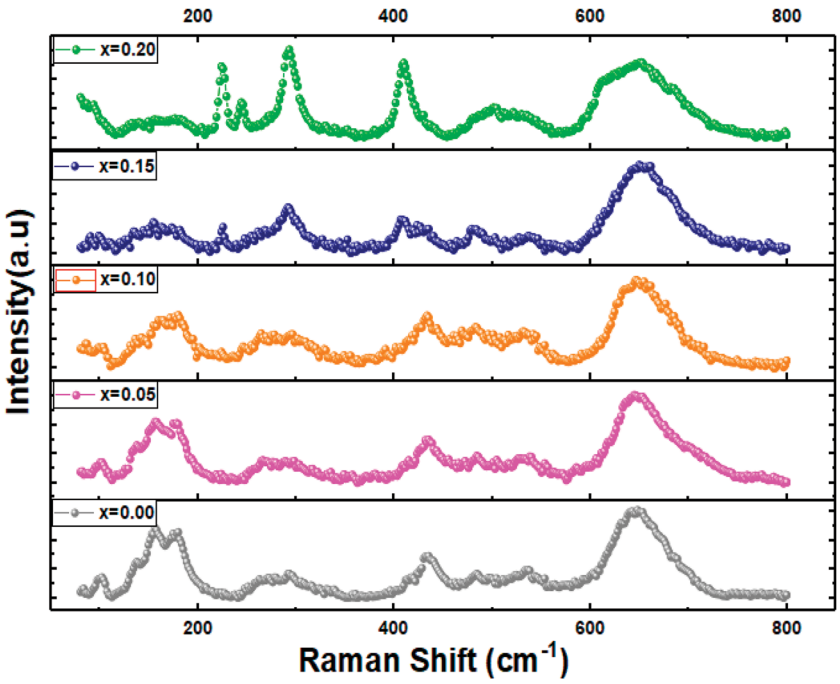

Fig. 5 Raman spectra of $La_{1-2x}Bi_xBa_xFeO_3$ (x = 0.0, 0.05, 0.1, 0.15 and 0.2) compounds.

 © 2021 The Author(s). Published by the Royal Society of Chemistry

Open Access Article. Published on 10 November 2021. Downloaded on 12/4/2025 4:48:14 PM.
This article is licensed under a Creative Commons Attribution-NonCommercial 3.0 Unported Licence.

the decrease of the formation of oxygen vacancies and the presence of the secondary phases for the compounds with the substitution amount with $x > 0.1$.[38]

Furthermore, the average crystallite size of the $La_{1-2x}Ba_x$-Bi_xFeO_3 nanoparticles was calculated using the Williamson Hall's method eqn (1).[27]

The value of D_{W-H} was calculated using the intercept of the linear fit of $(\beta \cos(\theta))$ *vs.* $(4 \sin(\theta))$ (Fig. 3). Accordingly, the calculated crystallite size values of the studied compounds were presented in Table 1. The variation of the crystallite size values is quite similar to the structural parameter trend with substitution.

3.2 Morphological study

The morphologies of the $La_{1-2x}Ba_xBi_xFeO_3$ nanostructures compounds obtained by the auto-combustion reaction are

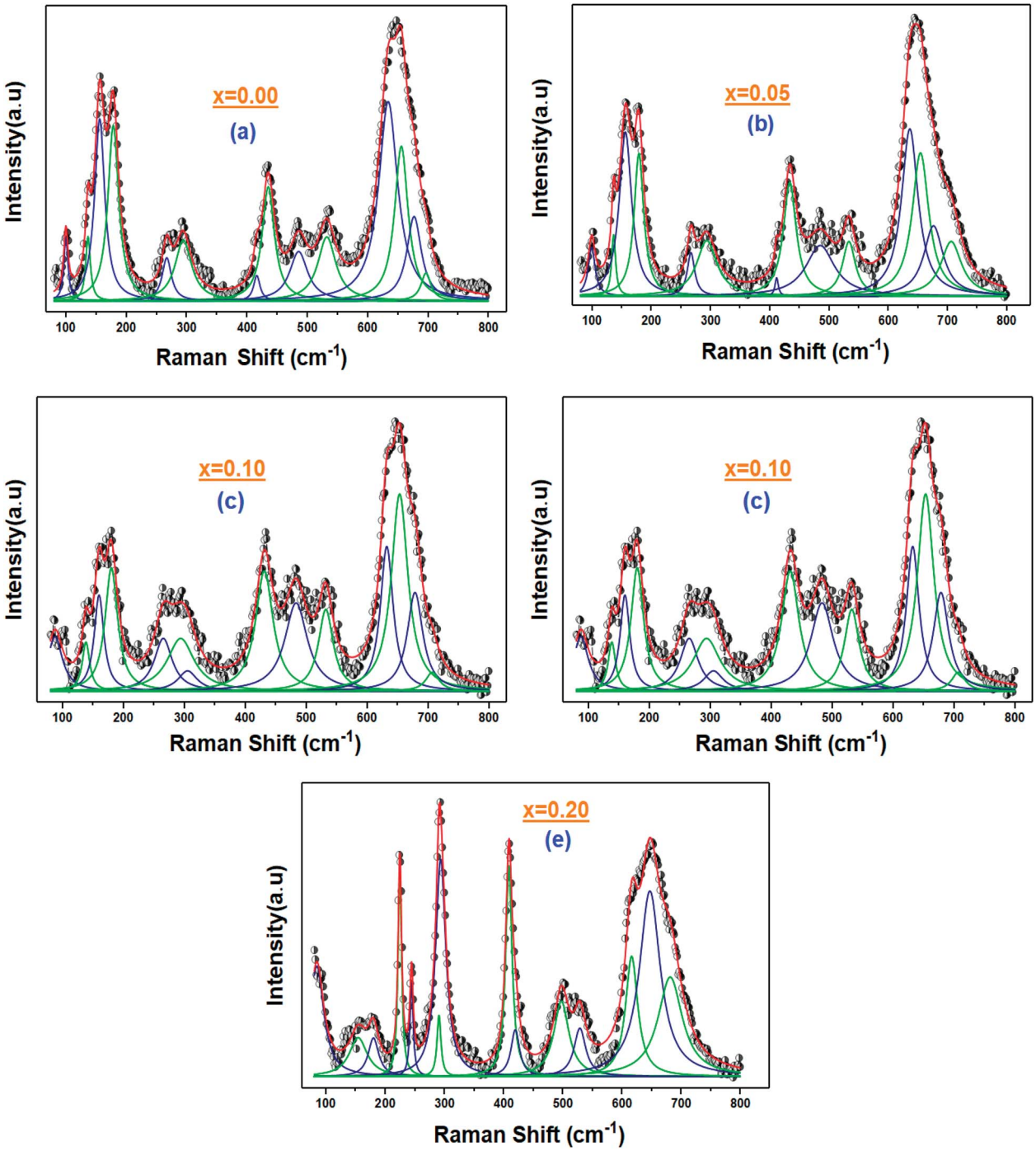

Fig. 6 (a–e) Fitting curves of the Raman signal for the $La_{1-2x}Ba_xBi_xFeO_3$ ($x = 0.0$, 0.05, 0.10, 0.15 and 0.20) ceramic samples with the Lorentzian line shapes.

Open Access Article. Published on 10 November 2021. Downloaded on 12/4/2025 4:48:14 PM.
This article is licensed under a Creative Commons Attribution-NonCommercial 3.0 Unported Licence.

examined by the SEM analysis (Fig. 4), which is a very useful tool to characterize the surface morphology and microstructure of our synthesized samples. The porous structure is seen in the SEM images; one can see that the grains show an irregular morphology.

The grain size distribution was calculated based on the SEM images and using the "*Image-J*" software. The obtained histogram for the $La_{0.8}Ba_{0.1}Bi_{0.1}FeO_3$ ($x = 0.1$) compound is illustrated in Fig. 4a. A Lorentzian adjustment was used to calculate the grain size of all samples. All the obtained grain size values are collected in Table 1, and the trend of these values with the substitution amount is in good agreement with that of crystallite size obtained from the structural study. However, we can note that the grain size values are much higher than those

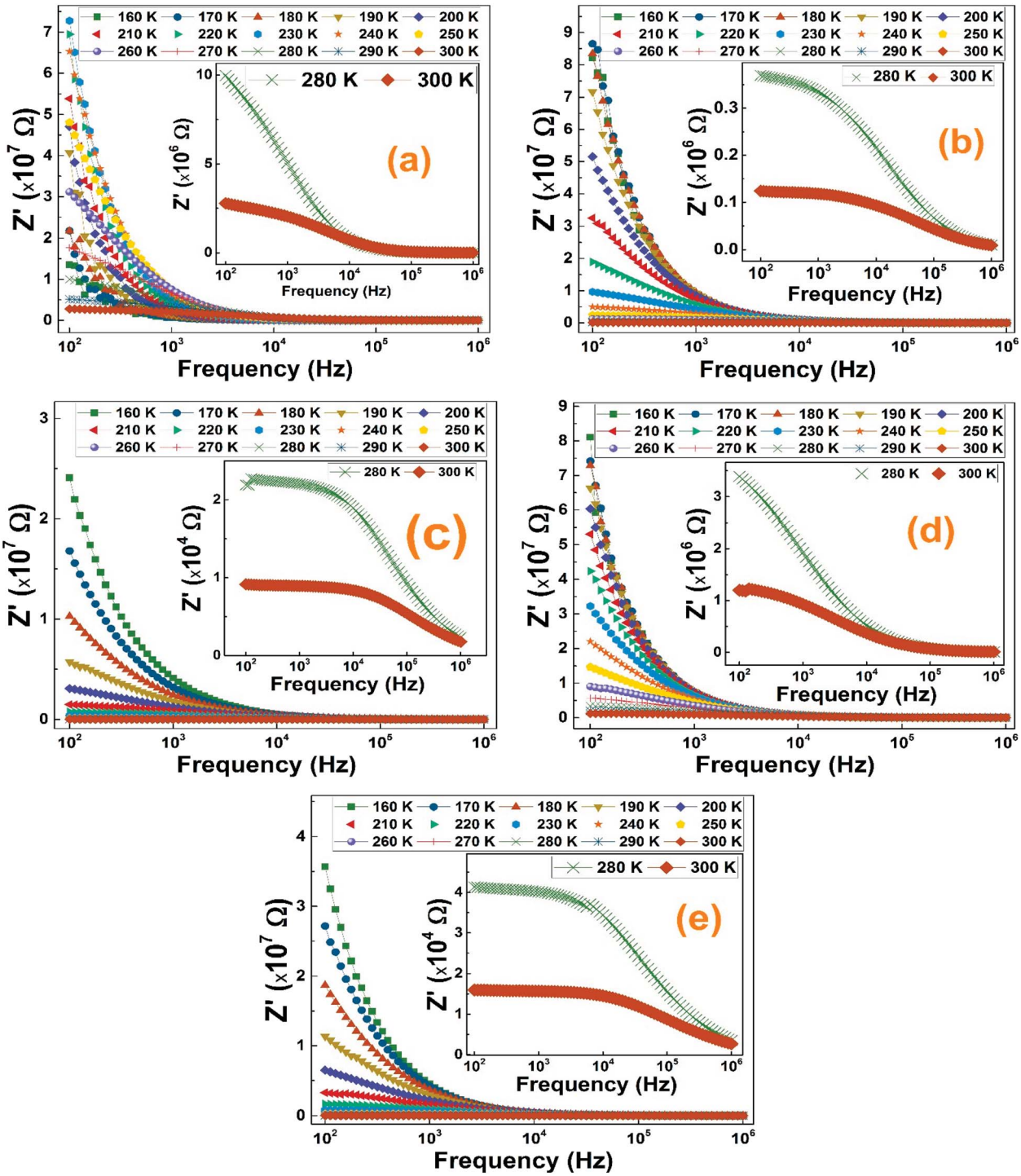

Fig. 7 (a–e) The frequency dependence of the real part of impedance at serval temperature of $La_{1-2x}Ba_xBi_xFeO_3$ ($x = 0.0$, 0.05, 0.10, 0.15 and 0.20) ceramic samples.

 © 2021 The Author(s). Published by the Royal Society of Chemistry

Open Access Article. Published on 10 November 2021. Downloaded on 12/4/2025 4:48:14 PM.
This article is licensed under a Creative Commons Attribution-NonCommercial 3.0 Unported Licence.

of crystallites which confirms that one grain is composed by several crystallites. On the other side, in order to confirm the existence of the elemental composition of our prepared ceramics, an Energy Dispersive X-ray Spectroscopy (EDS) has been used. The spectra illustrated in Fig. 4b shows the presence of the peaks corresponding to all starting elements for the preparation of $La_{1-2x}Ba_xBi_xFeO_3$ compounds (La, Ba, Bi, Fe and O). One can see that the carbon (C) and aluminum (Al) elements are also present in the spectrum of all samples. The presence of these two elements can be explained by the carbon tape used in the EDS analysis and the Al peak it comes from the aluminum used to cover the beaker during the auto-combustion reaction.

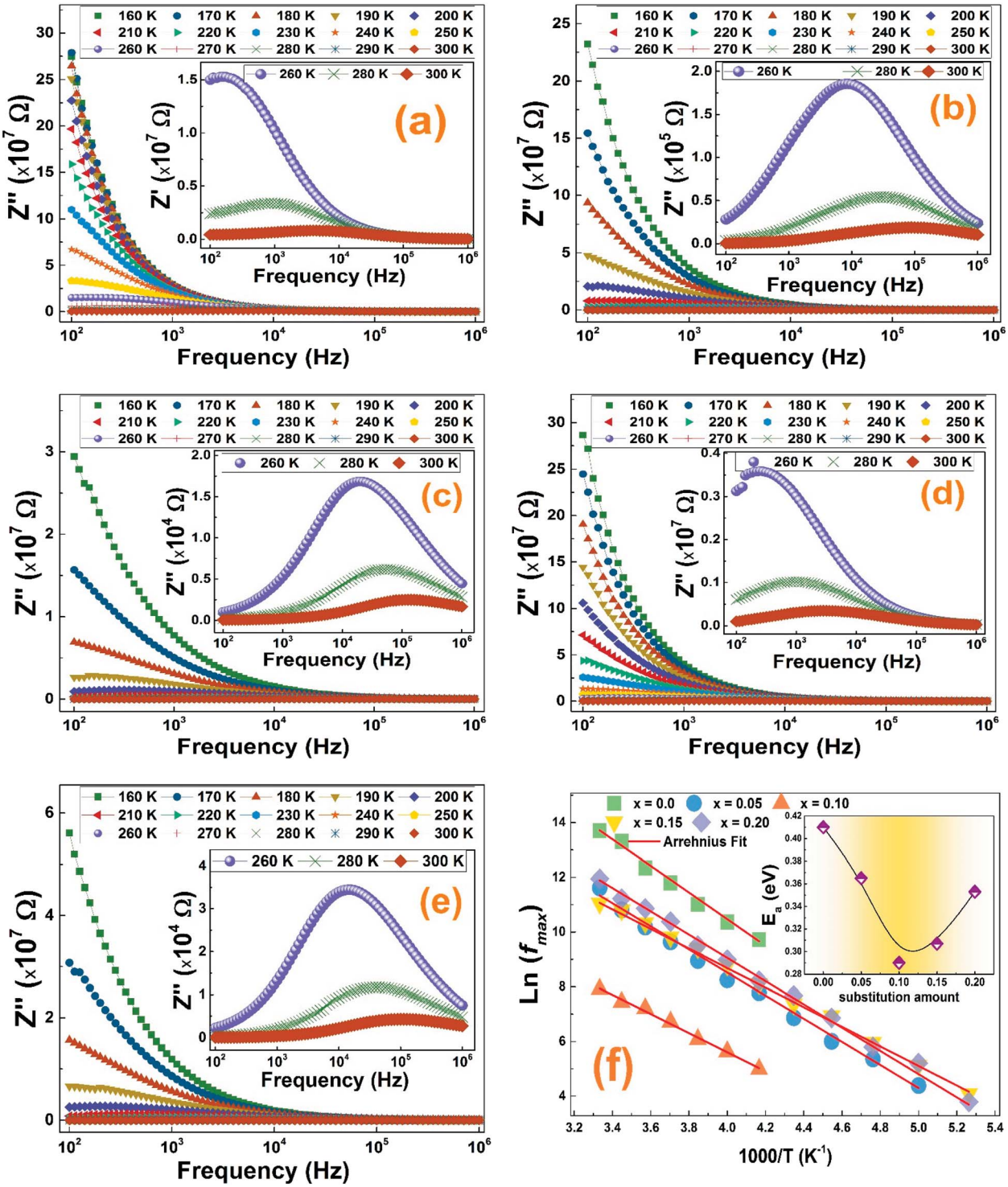

Fig. 8 (a–e) The frequency dependence of the imaginary part of impedance at serval temperature of $La_{1-2x}Ba_xBi_xFeO_3$ ($x = 0.0$, 0.05, 0.10, 0.15, and 0.20) ceramic samples, respectively. (f) Arrhenius plots and activation energies as function of the substitution amount.

Open Access Article. Published on 10 November 2021. Downloaded on 12/4/2025 4:48:14 PM.
This article is licensed under a Creative Commons Attribution-NonCommercial 3.0 Unported Licence.

These results confirm well the absence of chemical element losses during the preparation steps.

Furthermore, the atomic weight percentages of our compounds are given in Table 2. The elemental composition values are almost in good agreement with stoichiometric chemical composition.

3.3. Raman scattering spectra

Raman spectroscopy is known as a powerful tool for phase structural analysis and it is more sensitive than the XRD because its excitation energy is less penetrating than X-ray.[39] It was reported that the Raman spectra of pure and doped $LaFeO_3$ compounds with the orthorhombic structure and *Pnma* space group present 24 active Raman modes given by eqn (2).[28]

Fig. 5 shows the RT Raman spectra of $La_{1-2x}Ba_xBi_xFeO_3$ (x = 0.0, 0.05, 0.10, 0.15 and 0.20) materials, which reveals the presence of almost the Raman actives modes of the pure $LaFeO_3$ ($x = 0.0$) sample. Also, these observed Raman peaks are in good agreement with those reported in our previous work for the case of LBBFO-AC and LBBFO-SG compounds[25].

The four Raman modes selected above are: the modes present below 200 cm^{-1} which are caused by the La vibrations and are known as mode (A), modes between 200 cm^{-1} and 300 cm^{-1} related to the oxygen octahedral tilt modes (T) in La, modes present between 400 cm^{-1} and 450 cm^{-1} attributed to the oxygen octahedral bending vibrations (B) and finally the modes above 500 cm^{-1} identified by the oxygen stretching vibrations (S).[40] However, we must note that no other additional peaks corresponding to the secondary phase were found like in XRD patterns.

The Raman peaks of the prepared samples were fitted using the Lorentzian functions (Fig. 6). As we can see, the Ba^{2+} and Bi^{3+} doping ions affect the "La" vibration modes (A). Further, the shift of some Raman signals towards the lower or the higher wavenumber and the variation in their intensities are influenced by the crystallite size, lattice size and defects.[41]

3.4. Complex impedance spectra

We have measured the reel and imaginary parts of the complex electrical impedance of all $La_{1-2x}Ba_xBi_xFeO_3$ ($x = 0.0$, 0.05, 0.10, 0.15 and 0.20) compounds at several temperatures in the frequency range of 100 Hz to 1 MHz in order to study their relaxation process. Fig. 7 illustrates the variation of real part of the impedance (Z') of $La_{1-2x}Ba_xBi_xFeO_3$ ($x = 0.0$, 0.05, 0.1, 0.15 and 0.2) compounds with respect to frequency at selected temperature range. For all temperatures, the (Z') values are found to decrease with increasing frequency. The maximum values of Z' of all compounds have been recorded at low-frequency range which may indicate an accumulation of a space charge polarization.[42] Moreover, it was also noticed that the (Z') values decrease with the increase of temperature, indicating the existence of a negative thermal coefficient of resistance (NTCR) behavior at the lower frequency region.[43]

The merging trend of all compounds graphs at high frequencies reveals the release of space charge and a reduction of barrier in materials which is always accompanied by an increase of the electrical conductivity as it will be proved in the ac-conductivity section.[44] Normally, for known temperature, the increasing trend of the Z' values with increasing frequency presents an inflexion point where the imaginary part graph shows a relaxation peak.[45]

To better understand the relaxation process throughout the $La_{1-2x}Ba_xBi_xFeO_3$ ($x = 0.0$, 0.05, 0.1, 0.15 and 0.2) compounds, we plotted in Fig. 8 the frequency and temperature dependence of the imaginary part of the complex electrical impedance Z''.

As we can see in Fig. 8, for all compounds, Z'' increases when increasing the frequency to reaches a maximum value, indicating the presence of relaxation phenomenon in these nanoparticles, before it decreases quickly.[46] The merging of all curves at high frequency shows a possible release of space charge.[47] Furthermore, two characteristic phenomena have been noticed in Z'' graphs of all compounds: the increase in temperature is accompanied by a decrease of the peak heights and alongside, a shift of the peak positions towards higher frequency. This can be related to the existence of a thermally activated dielectric relaxation in the studied compounds.

For all compounds, the activation energy (E_a) was extracted by plotting the change of $\ln(f_{max})$ *versus* the inverse of temperature ($1/T$) as shown in Fig. 8(f) with respect to the Arrhenius equation described by eqn (3).

The extracted activation energy (E_a) values, from the slope of linear adjustment of the $\ln(f_{max})$ *vs.* ($1/T$) curves, and the calculated E_a values are collected in Table 3. As presented in the inset of Fig. 8(f), the activation energy was affected by the substitution amount: it decreases until a minimum for the

Table 3 The values of the activation energy of $La_{1-2x}Ba_xBi_xFeO_3$ (x = 0.00, 0.05, 0.10, 0.15 and 0.20) compounds calculated from the dielectric parameters

		E_a (eV)				
	Contribution	$x = 0.00$	$x = 0.05$	$x = 0.10$	$x = 0.15$	$x = 0.20$
(Z'') *vs.* frequency		0.410	0.365	0.29	0.307	0.353
(M'') *vs.* frequency	Grain boundary	0.401	0.341	0.278	0.282	0.302
	Grain	—	0.162	0.142	0.179	0.246
(Z'') *vs.* (Z')	Grain boundary	0.413	0.281	0.181	0.258	0.266
	Grain	0.117	0.223	0.146	0.228	0.246
$\ln(\sigma_{ac} \times T)$ *vs.* $1000/T$		0.396	0.358	0.289	0.324	0.353

 © 2021 The Author(s). Published by the Royal Society of Chemistry

Open Access Article. Published on 10 November 2021. Downloaded on 12/4/2025 4:48:14 PM.
This article is licensed under a Creative Commons Attribution-NonCommercial 3.0 Unported Licence.

compound with $x = 0.10$ and then increases for further substitution amount.

In order to know the origin of the relaxation peaks that appeared in the imaginary part of the impedance curves and to better study separately the dielectric properties of all contributions of the studied compounds, we modeled our systems using an equivalent electrical circuit to adjust the Nyquist Cole/Cole plots at different temperatures. The Nyquist plots of $La_{1-2x}Ba_xBi_xFeO_3$ ($x = 0.0$, 0.05, 0.10, 0.15 and 0.20) compounds are presented in Fig. 9. It is clearly seen that, for all compounds, when increasing temperature, the diameter of semicircles decreases indicating an increase of the total electrical

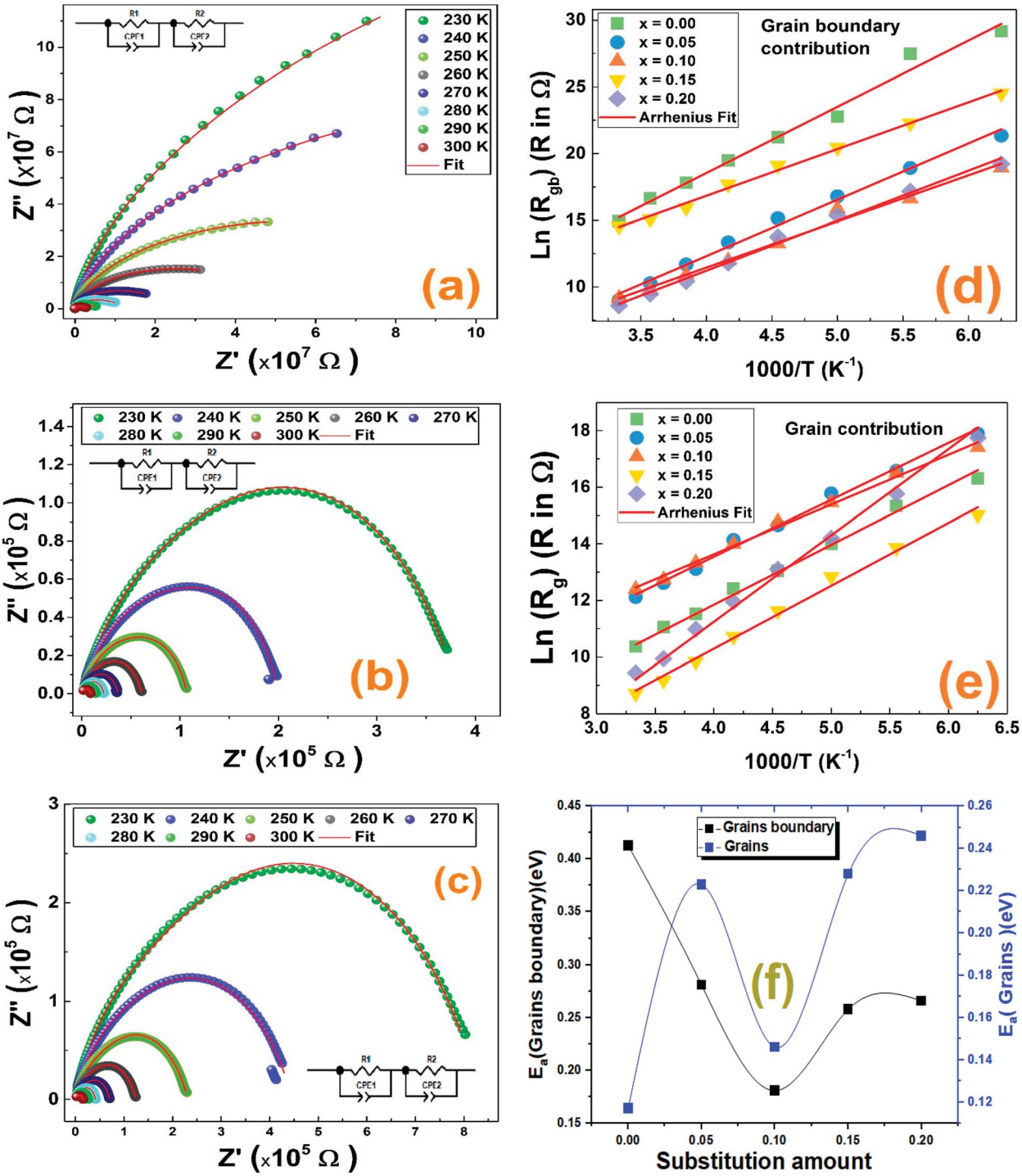

Fig. 9 (a–c) The impedance Nyquist plots of the $La_{1-2x}Ba_xBi_xFeO_3$ ($x = 0.0$, 0.10, 0.20) Compounds. (d) and (e) the Arrhenius plots ($\ln(f_{max})$ *vs.* $1000/T$) of the grain boundary and grain contributions, respectively. (f) The variation of the activation energy as function of the substitution amount for grain and grain boundaries contributions.

Open Access Article. Published on 10 November 2021. Downloaded on 12/4/2025 4:48:14 PM.
This article is licensed under a Creative Commons Attribution-NonCommercial 3.0 Unported Licence.

Table 4 Values of electrical parameters deduced from the Nyquist for $La_{1-2x}Ba_xBi_xFeO_3$ ($x = 0.00$; 0.50; 0.10; 0.15; 0.20): grain contribution

Grain contribution															
	$x = 0.00$			$x = 0.05$			$x = 0.10$			$x = 0.15$			$x = 0.20$		
T (K)	R_g (10^5 Ω)	QPE_g (10^{-10})	α	R_g (10^5 Ω)	QPE_g (10^{-10})	α	R_g (10^5 Ω)	QPE_g (10^{-10})	α	R_g (10^5 Ω)	QPE_g (10^{-10}F)	α	R_g (10^5 Ω)	QPE_g (10^{-10})	α
160	120.549	1.25	1	589.884	0.052	0.85	364.214	0.24	1.03	33.556	2.42	1.02	508.993	1.16	1.02
180	45.975	1.15	1.03	159.152	0.019	1	145.526	0.86	1	10.576	0.273	0.86	70.538	1.96	1
200	11.984	1.85	1	71.452	0.099	0.78	51.810	0.0612	0.86	3.761	0.956	0.56	14.701	0.064	0.81
220	4.616	0.19	1	23.316	0.012	0.76	26.372	0.105	0.78	1.124	0.010	0.73	4.913	0.056	0.77
240	2.479	0.30	0.97	13.864	0.077	0.72	11.940	0.92	0.77	0.453	0.053	0.69	1.555	0.33	0.83
260	1.018	15.06	1	4.975	0.28	0.73	6.204	0.74	0.71	0.187	0.015	0.71	0.588	0.16	0.78
280	0.634	13.10	0.86	3.015	7.26	0.74	3.410	0.97	0.74	0.096	0.40	0.77	0.207	1.03	0.85
300	0.321	14.89	0.87	1.839	0.10	0.72	2.428	0.142	0.75	0.061	0.043	0.73	0.126	1.48	0.84

Table 5 Values of electrical parameters deduced from the Nyquist for $La_{1-2x}Ba_xBi_xFeO_3$ ($x = 0.00$, 0.50, 0.10, 0.15 and 0.20): grain boundary contribution

Grain boundary contribution															
	$x = 0.00$			$x = 0.05$			$x = 0.10$			$x = 0.15$			$x = 0.20$		
T (K)	R_{gb} (10^7 Ω)	QPE_{gb} (10^{-12})	α	R_{gb} (10^7 Ω)	QPE_{gb} (10^{-12})	α	R_{gb} (10^7 Ω)	QPE_{gb} (10^{-12})	α	R_{gb} (10^7 Ω)	QPE_{gb} (10^{-12}F)	α	R_{gb} (10^7 Ω)	QPE_{gb} (10^{-12})	α
160	463 000	2.417	0.750	187.239	0.416	0.919	16.718	0.5276	0.66	4470.142	0.809	0.550	22.142	0.277	0.611
180	85 480	2.370	0.689	16.501	0.886	0.655	1.642	0.769	0.72	474.9927	1.698	0.570	2.84	0.496	0.620
200	779	6.188	0.591	1.967	2.308	0.577	0.774	1.233	0.72	76.4	2.330	0.604	0.47	1.470	0.593
220	164.8	7.950	0.550	0.381	4.909	0.591	0.057	2.842	0.65	19.9	2.241	0.722	0.0948	3.297	0.587
240	29.43	9.661	0.529	0.062	6.890	0.560	0.016	3.639	0.61	4.81	3.833	0.744	0.0134	4.170	0.605
260	5.41	13.822	0.508	0.012	8.540	0.589	0.0054	4.652	0.60	0.84	4.244	0.713	0.00336	6.940	0.611
280	1.7	15.161	0.516	0.00294	9.651	0.583	0.00162	5.761	0.58	0.36	4.976	0.629	0.00132	7.050	0.639
300	0.31	18.830	0.527	8.225×10^{-4}	10.840	0.632	9.539×10^{-4}	52.76	0.66	0.21	6.036	0.717	5.420×10^{-4}	10.508	0.608

© 2021 The Author(s). Published by the Royal Society of Chemistry

Open Access Article. Published on 10 November 2021. Downloaded on 12/4/2025 4:48:14 PM.
This article is licensed under a Creative Commons Attribution-NonCommercial 3.0 Unported Licence.

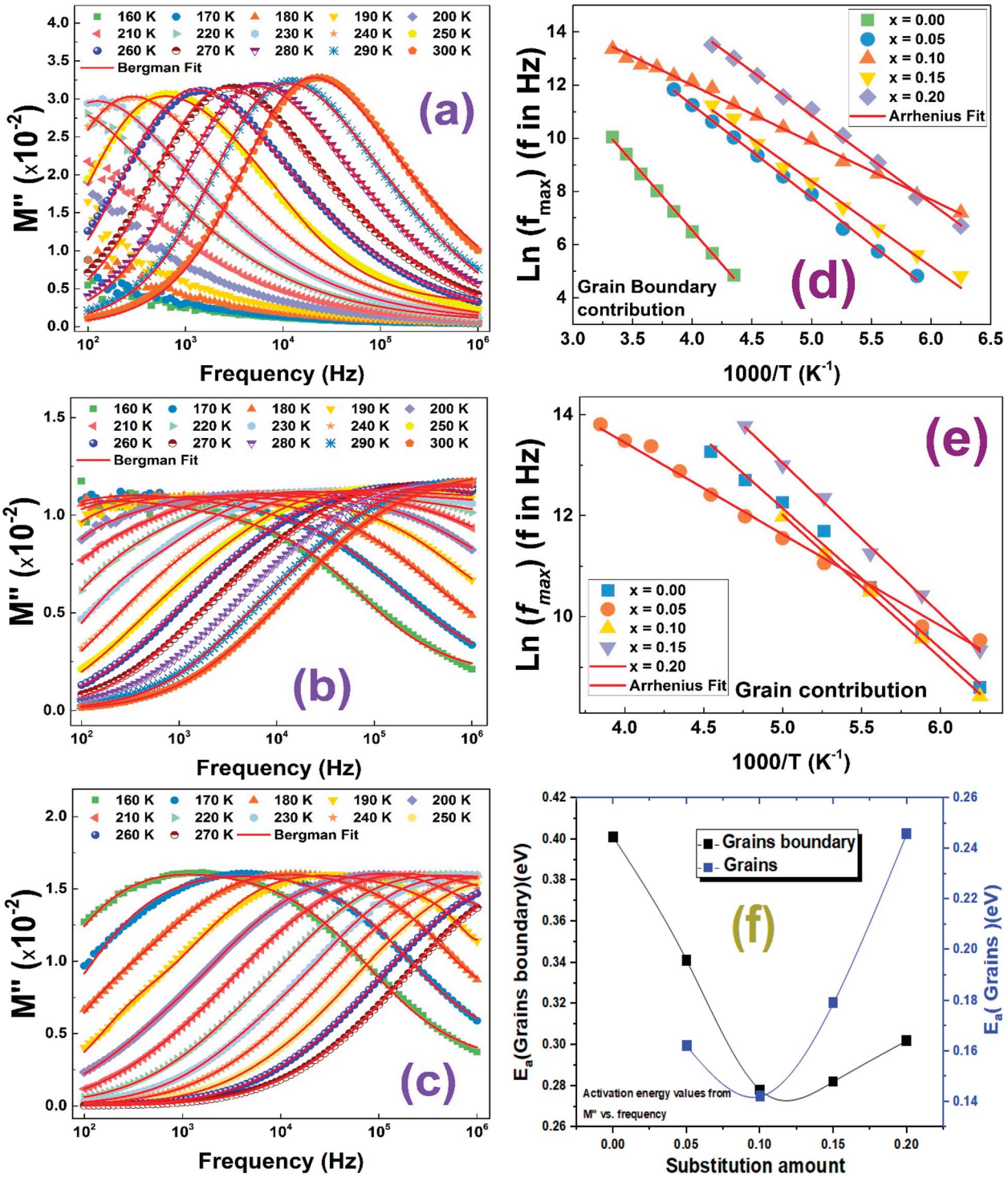

Fig. 10 (a–c) The Bergman fitted M'' curves of the $La_{1-2x}Ba_xBi_xFeO_3$ ($x = 0.00$, 0.05, 0.10, 0.15 and 0.20) compounds. (d) and (e) the Arrhenius plots ($\ln(f_{max})$ *vs.* $1000/T$) of the grain boundary and grain contributions, respectively. (f) The variation of the activation energy as function of the substitution amount for grain and grain boundaries contributions.

conductivity.[48] Obviously, the Nyquist plots are consistent of more than semicircle proving the existence of more than one contribution. We have used the Z-view software to adjust these Nyquist plots for all compounds.[49] The adequate electrical circuit consists of series combination of two resistors R1 and R2, where each one is in parallel with constant phase element (Q1 and Q2) as presented in the inset of all Nyquist plots in Fig. 9. This confirms well the existence of the grain and grain boundary contributions in the studied compounds at low and high frequency ranges, respectively.

Open Access Article. Published on 10 November 2021. Downloaded on 12/4/2025 4:48:14 PM.
This article is licensed under a Creative Commons Attribution-NonCommercial 3.0 Unported Licence.

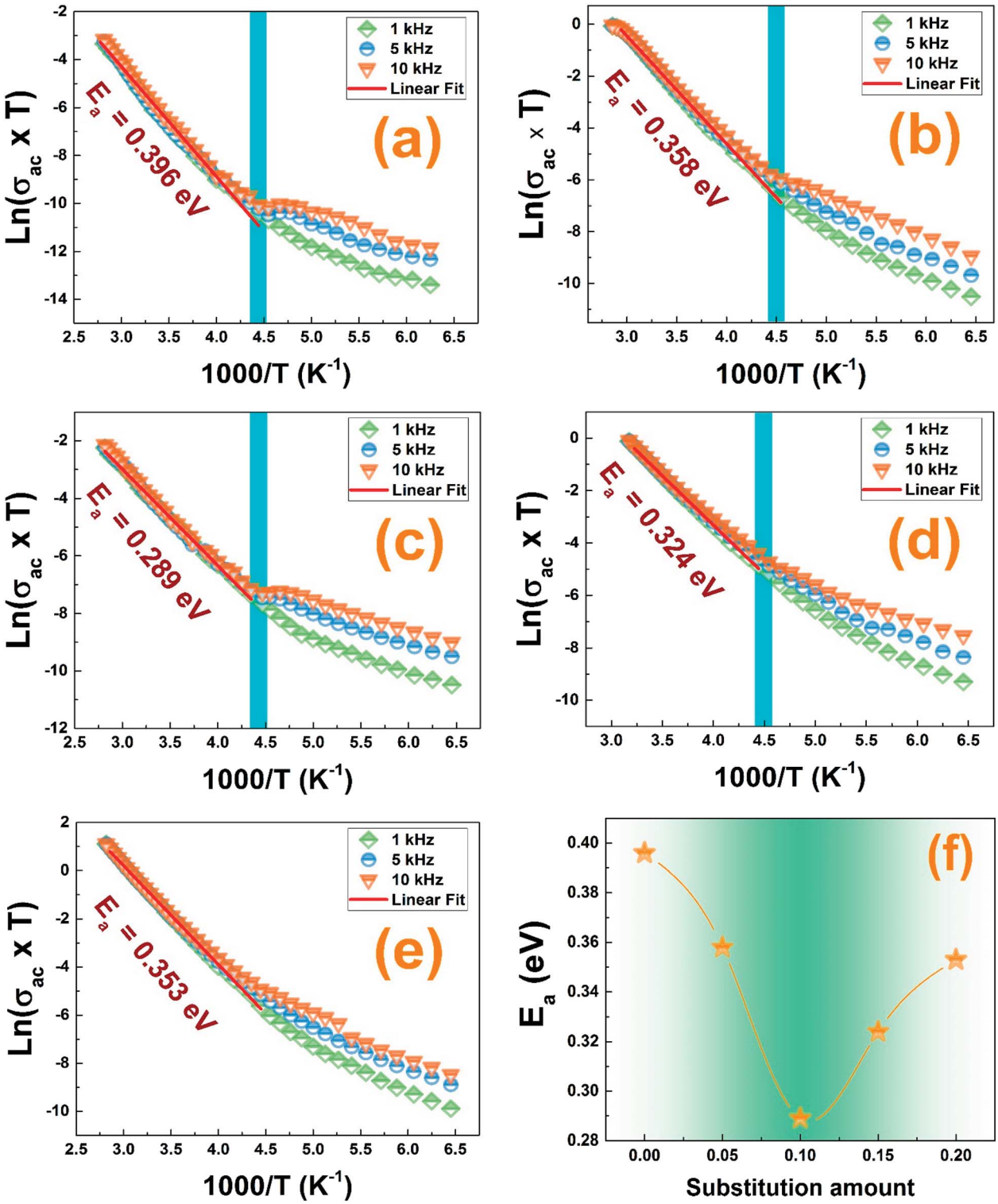

Fig. 11 (a–e) Variation of $\ln(\sigma_{ac} \times T)$ *vs.* $1000/T$ for $La_{1-2x}Ba_xBi_xFeO_3$ (x = 0.00, 0.05, 0.10, 0.15 and 0.20) compounds, respectively; (f) the variation of the activation energy as function of the substitution amount for grain and grain boundaries contributions.

Thus, the total conductivity has both the grain and grain boundary contributions. These results are quite similar to those of doped lanthanum ferrite systems[50].

The values of the obtained fitting parameters are listed in Tables 4 and 5. As one can see, the resistance of both contributions decreases with increasing temperature proving the semiconducting criteria of the studied materials. Moreover, the

 © 2021 The Author(s). Published by the Royal Society of Chemistry

Open Access Article. Published on 10 November 2021. Downloaded on 12/4/2025 4:48:14 PM.
This article is licensed under a Creative Commons Attribution-NonCommercial 3.0 Unported Licence.

resistance of the grain boundary contribution is higher than of the grain one which is in good agreement with previous results of ferroic perovskite materials.[51,52] Also, we can deduce that the values of the alpha (α) parameter are around the unite for all compounds at the used temperature range which means that the QPE element is very close to a capacitance. We have plotted the logarithmic resistance values of both contributions as function of the inverse of temperature ($1/T$) with respect of the Arrhenius power law eqn (4), in order to evaluate the effect of the substitution on the activation energy corresponding to grain and grain boundary contributions.

Where R_0 is the characteristic resistance and E_a is the activation energy. Related to eqn (4), the plots of $\ln(R_{g/\,bg})$ *vs.* $1000/T$ (Fig. 9) would be linear and one can estimate the E_a using the slope of the linear fit. The calculated activation energy values of grain and grain boundary contributions are collected in Table 3. It was reported that the insertion of Bi^{3+} in the A site of $LaFeO_3$ acts to decrease the activation energy values.[53] The behavior of activation energy (Fig. 9(f)) and resistance are quite similar to the crystallite size behavior previously calculated by the Williamson–Hall formalism; the compound with $x = 0.10$ presents the lowest value of resistance and activation energies of both grain and grain boundary contributions. We have previously proved the high utility of the $La_{0.8}Ba_{0.1}Bi_{0.1}FeO_3$ compound ($x = 0.10$) for gas sensing applications.[26]

3.5. Complex electrical modulus analysis

The complex modulus analysis is a very useful characterization technique used to differentiate the dielectric relaxations of grain (bulk) and grain boundary contributions. The variation of the imaginary parts of the modulus (M'') of all compounds as function of the frequency, over the 150–300 K temperature range, are shown in Fig. 10.

It is important to notice that for the compound with $x = 0.00$ (Fig. 10(a)), only one relaxation peak has been detected in the selected temperature range, while when introducing barium and bismuth ions in A-site of the lanthanum ferrite material, a second relaxation has been identified. We can mention also that all relaxation peaks shift towards higher frequencies when increasing the temperature which confirms well the thermally activated relaxation processes.[54] It is important to note the existence of a pure conduction process occurring generally at low frequencies where ions move freely on long-distance.[55] When relaxation peaks shift to high frequencies, almost ions will be confined in the localized motion corresponding to the short-distance carriers hopping process.[56–58]

To further qualify the relaxation process of different contributions on the $La_{1-2x}Ba_xBi_xFeO_3$ ($x = 0.0$, 0.05, 0.10, 0.15 and 0.20) compounds, we have adjusted the M'' experimental data using eqn (5).[29]

To calculate the activation energies of both contributions, we used the obtained values of f_{max} and we plotted the variation of $\ln(f_{max})$ as function of $1000/T$ as shown in Fig. 10(d) and (e). The calculated activation energy values are plotted in Fig. 10(f). We found that these values are in good agreement with those previously deduced from the resistance value (Fig. 9(f)). Once again, the compound with $x = 0.10$ presents the lowest activation energy for grain and boundary grain contributions. Accordingly, we confirm the important utility of substituting La^{3+} ions by together Ba^{2+} and Bi^{3+} ones with a substitution

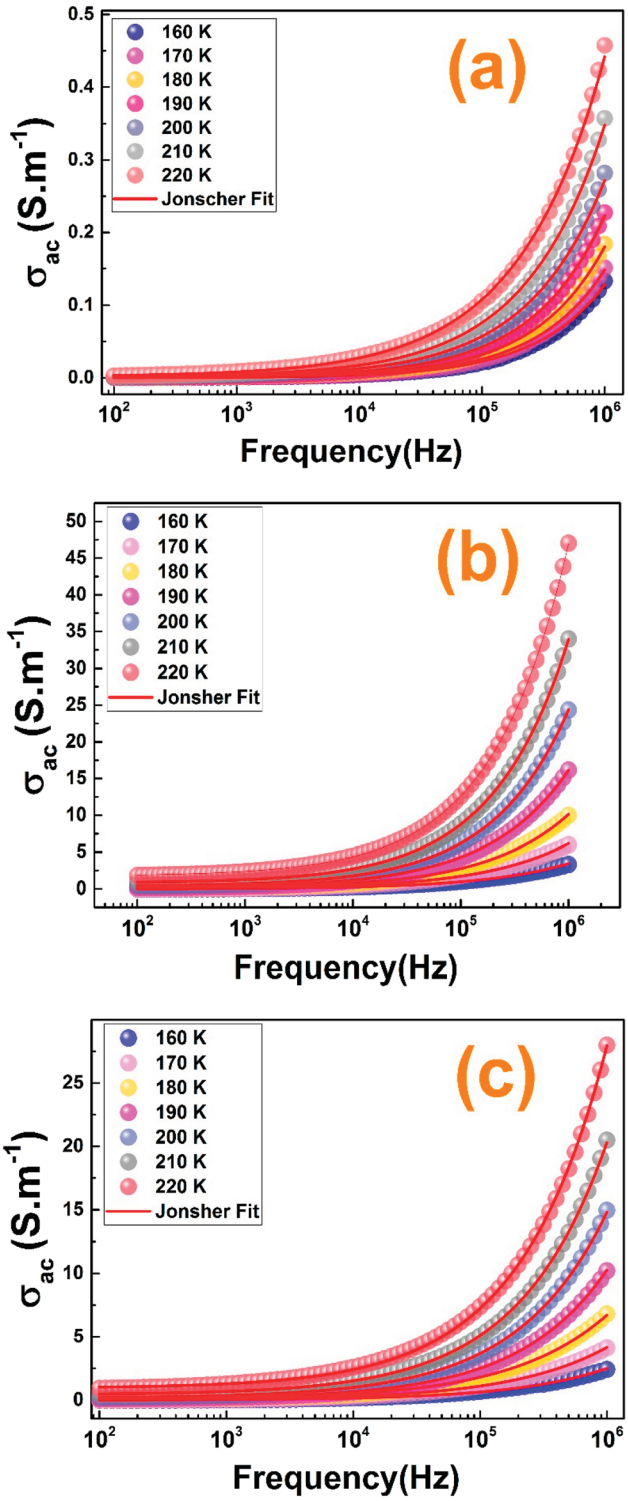

Fig. 12 (a–c) The ac-conductivity adjustment results with the Jonscher's power law of the $La_{1-2x}Ba_xBi_xFeO_3$ ($x = 0.00$, 0.10 and 0.20) compounds, respectively.

Open Access Article. Published on 10 November 2021. Downloaded on 12/4/2025 4:48:14 PM.
This article is licensed under a Creative Commons Attribution-NonCommercial 3.0 Unported Licence.

amount lower than 10% that decreases the activation energy and the crystallite size values.

3.6. The electrical conductivity

The electrical conductivity is helpful to reveal more information about the nature of the conduction mechanism. We plotted in Fig. 11 the logarithmic variation of the ac-conductivity multiplied by temperature ($\ln(\sigma_{ac}*T)$) as function of $1000/T$ at the selected frequencies. Two distinguish regions are clearly seen for all studied compounds; low and high temperature ranges. At high temperature region, the ac-conductivity of all compounds was found to depend only on temperature; does not depend on the frequency and it increases when increasing temperature indicating a thermally activated conduction mechanism.[59] While at low temperature region, the ac-conductivity depends on both temperature and frequency. It increases with the rise in temperature for each frequency and also it rises when increasing frequency for a given temperature as shown in Fig. 11. As known, for the large polaron hopping process, the ac conductivity decreases with frequency while it increases for the small polaron hopping process.[60,61] For $T < 222$ K, one can see that the increase of frequency results in an enhancement of the ac-conductivity. This confirms well that at low temperatures, the conduction process occurs essentially by the small polaron hopping between localized states as we will study in detail in the following part using Jonscher's power law.

In the high temperature region, the plots of all the frequencies seem to merge into a single curve. We have calculated the activation energy in the region of temperature $T > 222$ K using the Arrhenius' law given by eqn (6).[31]

The activation energy values, deduced from the slopes of each linear adjustment, are collected in Table 3. These obtained values are in good agreement with those previously calculated which suggests that the relaxation process and the electrical conductivity are attributed to the same type of charge carriers, specifically the jump of electrons between the states of iron. The decrease of the activation energy values, when introducing less than 10% of barium and bismuth ions, can be correlated with the decrease of crystallites size. When the substitution amount is higher than 10%, the increase of the crystallites size is followed by an enhancement of the activation energies.

Fig. 12 shows the frequency dependence of the electrical conductivity for our prepared ceramics at selected temperatures. It is observed that the ac conductivity curves increase with the rise of the frequency for all the samples which confirms that the conduction is due to the small polaron hopping process.[60,61] We can distinguish two regions with the variation of the frequency: (R1) is a plateau region and (R2) is a dispersion region. For the plateau, detected at low frequency region and corresponding to σ_{dc}, the conductivity increase, with the rise of the temperature, indicates that the electrical conductivity is a thermally activated process and the conductivity is independent of frequency. The dispersion region at high frequency range corresponds to the ac conductivity σ_{ac}. Related to Jonscher's power law, this frequency dependence behavior in this region can be due to the relaxation phenomena arising due to the hopping of mobile charge carriers.[62] For more information about the conduction process in our compounds, the analysis is done by Jonscher's power law given by eqn (7).[32]

Fig. 12 shows the well-fitting curves of the conductivity. The value $s \leq 1$ indicates a translational motion with a sudden hopping and the value $s > 1$ means the presence of a localized hopping.[63] For our samples, the s values are found to vary in the range of 0–1. So, we can confirm the presence of a translational motion with a sudden hopping in our compounds.

To determine the predominant conduction process for our compounds, we examined the variation of the parameter "s" as function of the temperature plotted as shown in Fig. 13. Different models have been suggested to describe the behavior of the exponent "s", for instance, the Small Polaron Tunneling (NSPT) model, where the exponent "s" increases with the rise of the temperature,[64] for the Quantum Mechanical Tunneling (QMT) model, the exponent "s" is independent of temperature and is almost equal to 0.8,[65] the Correlated Barrier Hopping (CBH) model where "s" decreases with the rise of the temperature[66] and the Overlapping Large-Polaron Tunneling (OLPT),[67] where the exponent s decreases with the rise of temperature

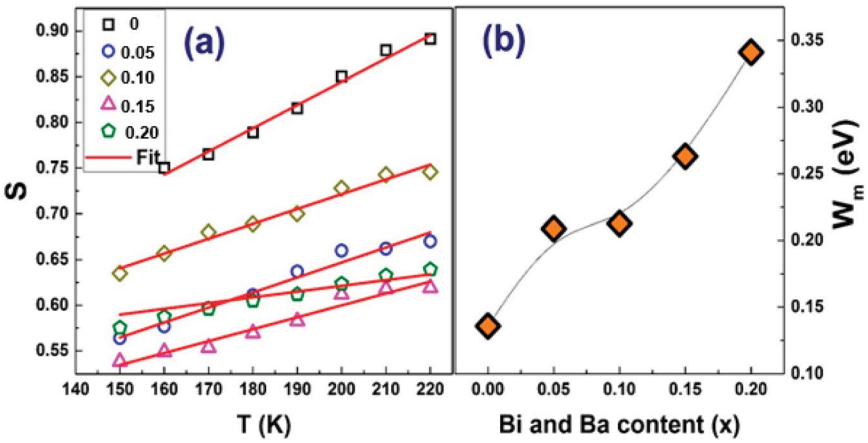

Fig. 13 (a) Variation of the exponent of Jonscher's power law S *vs.* T and (b) the W_m activation energies of the $La_{1-2x}Bi_xBa_xFeO_3$ ($x = 0.0$, 0.05, 0.1, 0.15 and 0.2) compounds.

 © 2021 The Author(s). Published by the Royal Society of Chemistry

Open Access Article. Published on 10 November 2021. Downloaded on 12/4/2025 4:48:14 PM.
This article is licensed under a Creative Commons Attribution-NonCommercial 3.0 Unported Licence.

predicting a minimum value and then increases again. For our samples, from the increase of the s values with the increase of the temperature, we can deduce that the most appropriate model for describing conductivity is the NSPT one.

According to the NSPT model, the exponent s is given by eqn (8).[33] For large values of $\frac{W_H}{k_B T}$,the equation given the exponent "s" eqn (8) is replaced by eqn (9).

Using the linear fit of the variation of "s" as function of the temperature, shown in Fig. 13(a), we have determined the values of W_H for our samples. From Fig. 13(b) illustrating the variation of the W_H values as function of the amount of substitution, it is clearly seen that the binding energy increases with the rise of the Ba and Bi contents.

4. Conclusion

In our study, the Bi and Ba doped $La_{1-2x}Ba_xBi_xFeO_3$ ($x = 0.00$, 0.05, 0.10, 0.15 and 0.2) compounds were synthesized by the auto-combustion route. The structural study by XRD measurements showed a *Pnma* orthorhombic structure with two secondary phases corresponding to the same space *I*4/*mmm* group for the compounds with $x = 0.15$ and 0.2. The XRD and SEM analyses revealed that the average crystallites and grains sizes of our samples change with the rise of the amount of the Bi and Ba. The vibrational study means by Raman spectroscopy, revealed the presence of all the vibration modes related to the *Pnma* space group. The impedance, the modulus and the ac conductivity data were carried out over a frequency and temperature range of (10^2 to 10^6 Hz) and (150 K to 300 K). The impedance analysis confirmed the presence of the relaxation phenomena and the contribution of grain boundary in transport properties. The evolution of the ac conductivity has proven a Jonscher's behavior where the exponent s showed an increasing trend for all samples (NSPT model). Besides, the activation energies obtained from the impedance, modulus and conductivity process are very close.

The study of the doping of barium and bismuth ions in the A site of $LaFeO_3$ helps us to explore this compound with improved structural, morphological and dielectric properties to be employed in modern-day applications like the gas sensor application which is already mentioned by our previous work.

Conflicts of interest

There are no conflicts to declare.

Acknowledgements

This work was supported by national funds from FCT – Fundação para a Ciência e a Tecnologia, I.P., within the projects UIDB/04564/2020 and UIDP/04564/2020.

References

1 L. B. Kong, Y. S. Shen and M. T. Wu, Study on sintering and gas sensing property of $LaFeO_3$ ceramics, in *Proceedings of the National 3rd Sensor Technology Conference*, Beijing, China, 1993, vol. 15–18, pp. 129–131.
2 F. J. Berry, X. Ren, J. R. Gancedo and J. F. Marco, ^{57}Fe Mössbauer Spectroscopy Study of $LaFe_{1-x}Co_xO_3$ ($x = 0$ and 0.5) Formed by Mechanical Milling, *Hyperfine Interact.*, 2004, **156**, 335–340.
3 S. Nakayama, $LaFeO_3$ perovskite-type oxide prepared by oxide-mixing, co-precipitation and complex synthesis methods, *J. Mater. Sci.*, 2001, **36**, 5643–5648.
4 Q. Zhang and F. Saito, Effect of Fe_2O_3 crystallite size on its mechanochemical reaction with La_2O_3 to form $LaFeO_3$, *J. Mater. Sci.*, 2001, **36**, 2287–2290.
5 E. M. Kostyukhin, A. L. Kustov and L. M. Kustov, One-step hydrothermal microwave-assisted synthesis of $LaFeO_3$ nanoparticles, *Ceram. Int.*, 2019, **45**, 14384–14388.
6 W. J. Zheng, R. H. Liu and D. K. Peng, *Mater. Lett.*, 2000, **43**, 19–22.
7 S. Phokha, S. Pinitsoontorn, S. Rujirawat and S. Maensiri, Polymer pyrolysis synthesis and magnetic properties of $LaFeO_3$ nanoparticles, *Physica B*, 2015, **476**, 55–60.
8 M. Sivakumar, A. Gedanken, W. Zhong, Y. H. Jiang, Y. W. Du, I. Brukental, D. Bhattacharya, Y. Yeshurun and I. Nowik, Sonochemical synthesis of nanocrystalline $LaFeO_3$, *J. Mater. Chem.*, 2004, **14**, 764–769.
9 W. Azouzi, W. Sigle, H. Labrim and M. Benaissa, *Mater. Sci. Semicond. Process.*, 2019, **104**, 1046823.
10 A. Benali, M. Bejar, E. Dhahri, M. Sajieddine, M. P. F. Graça and M. A. Valente, Magnetic, Raman and Mössbauer properties of double-doping $LaFeO_3$ perovskite oxides, *Mater. Chem. Phys.*, 2015, **149–150**, 467–472.
11 I. Purnamasari, I. Farida, N. Nanang and A. Zhafirah, Crystal structure analysis of Lanthanum Orthoferrite doped Zirconium with sol–gel method for solar cell candidate, *J. Phys.: Conf. Ser.*, 2021, **1869**, 012197.
12 N. A. Sazelee, N. H. Idris, M. F. Md Din, M. S. Yahya, N. A. Ali and M. Ismail, $LaFeO_3$ synthesised by solid-state method for enhanced sorption properties of MgH_2, *Results Phys.*, 2020, **16**, 102844.
13 S. Ahmadi, M. Mesbah, C. Adaobi Igwegbe, C. Daniel Ezeliora, C. Osagie, N. A. Khan, G. L. Dotto and M. Hadi Dehghani, Sono electro-chemical synthesis of $LaFeO_3$ nanoparticles for the removal of fluoride: Optimization and modeling using RSM, ANN and GA tools, *J. Environ. Chem. Eng.*, 2021, **9**, 105320.
14 P. B. Koli, K. H. Kapadnis, U. G. Deshpande, B. P. More and U. J. Tupe, *Mater. Sci. Res. India*, 2020, **17**, 70–82.
15 C. Chen, K. B. Xu, Y. M. Cui and C. C. Wang, Polaronic relaxation in $LaFeO_3$, *Mater. Lett.*, 2012, **89**, 153.
16 J. Mizusaki, T. Sasamo, W. R. Cannon and H. K. Bowen, Electronic Conductivity, Seebeck Coefficient, and Defect Structure of $LaFeO_3$, *J. Am. Ceram. Soc.*, 1982, **65**, 363–368.
17 F. H. Taylor, J. Buckeridge, C. Richard and A. Catlow, Screening Divalent Metals for A- and B-Site Dopants in $LaFeO_3$, *Chem. Mater.*, 2017, **29**, 8147–8157.
18 N. Karthikeyan, R. Ramesh Kumar, G. Jaiganesh and K. Sivakumar, Thermoelectric power factor of $La_{0.9}M_{0.1}FeO_3$ (M = Ca and Ba) system: Structural, band

Open Access Article. Published on 10 November 2021. Downloaded on 12/4/2025 4:48:14 PM.
This article is licensed under a Creative Commons Attribution-NonCommercial 3.0 Unported Licence.

gap and electrical transport evaluations, *Physica B*, 2018, **529**, 1–8.

19 D. Triyono, I. Purnamasari and R. A. Rafsanjani, Effect of the Zr-Substitution on the Structural and Electrical Properties of $LaFeO_3$: XRD, Raman Scattering, SEM, and Impedance Spectroscopy Study, *Crystals*, 2020, **10**, 399.

20 C. Xueying, L. Shengli and Z. Xinde, Microstructure and electrical properties of $La_{1-x}Sr_xFeO_3$ (x = 0–0.6) film by a screen-printing method, *Mater. Lett.*, 2014, **130**, 267–270.

21 E. Cao, Y. Qin, T. Cui, L. Sun, W. Hao and Y. Zhang, Influence of Na doping on the magnetic properties of $LaFeO_3$ powders and dielectric properties of $LaFeO_3$ ceramics prepared by citric sol–gel method, *Ceram. Int.*, 2017, **43**, 7922–7928.

22 L. Li, H. Qin, C. Shi, L. Zhang, Y. Chen and J. Hu, CO_2 sensing properties of $La_{1-x}Ba_xFeO_3$ thick film and packed powder sensors, *RSC Adv.*, 2015, **5**, 103073–103081.

23 C. Yao, J. Meng, X. Liu, X. Zhang, F. Meng, X. Wu and J. Meng, Effects of Bi doping on the microstructure, electrical and electrochemical properties of $La_{2-x}Bi_xCu_{0.5}Mn_{1.5}O_6$ (x = 0, 0.1 and 0.2) perovskites as novel cathodes for solid oxide fuel cells, *Electrochim. Acta*, 2017, **229**, 429–437.

24 J. Meng, X. Liu, C. Yao, X. Liu, X. Zhang, F. Meng and J. Meng, Bi-doped $La_2ZnMnO_{6-\delta}$ and relevant Bi-deficient compound as potential cathodes for intermediate temperature solid oxide fuel cells, *Solid State Ionics*, 2015, **279**, 32–38.

25 E. M. Benali, A. Benali, M. Bejar, E. Dhahri, M. P. F. Graca, M. A. Valente and B. F. O. Costa, Effect of synthesis route on structural, morphological, Raman, dielectric, and electric properties of $La_{0.8}Ba_{0.1}Bi_{0.1}FeO_3$, *J. Mater. Sci.: Mater. Electron.*, 2020, **31**, 3197–3214.

26 E. M. Benali, A. Benali, M. Bejar, E. Dhahri, V. A. Khomchenko, L. Peng, J. Wu and B. F. O. Costa, Structural, morphological and excellent gas sensing properties of $La_{1-2x}Ba_xBi_xFeO_3$ ($0.00 \leq x \leq 0.20$) nanoparticles, *J. Alloys Compd.*, 2021, **883**, 160856.

27 N. S. Goncalves, J. A. Carvalho, Z. M. Lima and J. M. Sasaki, Size–strain study of NiO nanoparticles by X-ray powder diffraction line broadening, *Mater. Lett.*, 2012, **72**, 36–38.

28 I. S. Smirnova, *Physica B*, 1999, **262**, 247–261.

29 R. Bergman, General Susceptibility Functions for Relaxations in Disordered Systems, *J. Appl. Phys.*, 2000, **88**, 1356–1365.

30 V. Thakur, A. Singh, A. M. Awasthi and L. Singh, Temperature dependent electrical transport characteristics of $BaTiO_3$ modified lithium borate glasses, *AIP Adv.*, 2015, **5**, 087110.

31 M. Ganguli, M. Harish Bhat and K. J. Rao, Lithium ion transport in Li_2SO_4–Li_2O–B_2O_3 glasses, *Phys. Chem. Glasses*, 1999, **40**, 297.

32 A. K. Jonscher, Dielectric relaxation in solids, *J. Phys. D: Appl. Phys.*, 1999, **32**, 57–70.

33 A. Kahouli, A. Sylvestre, F. Jomni, B. Yangui and J. Legrand, Experimental and Theoretical Study of AC Electrical Conduction Mechanisms of Semicrystalline Parylene C Thin Films, *J. Phys. Chem. A*, 2012, **116**, 1051–1058.

34 L. Sangaletti, L. E. Depero, B. Allieri, P. Nunziante and E. Traversa, An X-ray study of the trimetallic $La_xSm_{1-x}FeO_3$ orthoferrites, *J. Eur. Ceram. Soc.*, 2001, **21**, 719.

35 H. M. Rietveld, A profile refinement method for nuclear and magnetic structures, *J. Appl. Crystallogr.*, 1969, **2**, 65–71.

36 J. Rodriguez-Carvajal, Recent advances in magnetic structure determination by neutron powder diffraction, *Phys. B*, 1993, **192**, 55–69.

37 Q. Yao, C. Tian, Z. Lu, J. Wang, H. Zhou and G. Rao, *Ceram. Int.*, 2020, **46**, 20472–20476.

38 P. Song, H. Qin, L. Zhang, K. An, Z. Lin, J. Hu and M. Jiang, The structure, electrical and ethanol-sensing properties of $La_{1-x}Pb_xFeO_3$ perovskite ceramics with $x \leq 0.3$, *Sens. Actuators, B*, 2005, **104**, 312–316.

39 J. Feng, T. Liu, Y. Xu, J. Zhao and Y. He, Effects of PVA content on the synthesis of $LaFeO_3$ *via* sol–gel route, *Ceram. Int.*, 2011, **37**, 1203–1207.

40 M. Romero, R. W. Gómez, V. Marquina, J. L. Pérez-Mazariego and R. Escamilla, Synthesis by molten salt method of the $AFeO_3$ system (A = La, Gd) and its structural, vibrational and internal hyperfine magnetic field characterization, *Physica B*, 2014, **443**, 90–94.

41 M. Scepanovic, M. Grujic-Brojcin, Z. Dohcevic-Mitrovic and Z. V. Popovic, Investigation of vibrational and electronic properties of oxide nanopowders by spectroscopic methods, *J. Phys.: Conf. Ser.*, 2010, **253**, 012015.

42 P. Dhak, D. Dhak, M. Das, K. Pramanik and P. Pramanik, Impedance spectroscopy study of $LaMnO_3$ modified $BaTiO_3$ ceramics, *J. Mater. Sci. Eng. B*, 2009, **164**, 165–171.

43 B. Bechera, P. Nayak and R. N. P. Choudhary, Impedance spectroscopy study of $NaBa_2V_5O_{15}$ ceramic, *J. Alloys Compd.*, 2007, **436**, 226–232.

44 S. Gowreesan and A. R. Kumar, Effects of Mg^{2+} ion substitution on the structural and electric studies of spinel structure of $Co_{12x}Mg_xFe_2O_4$, *J. Mater. Sci.: Mater. Electron.*, 2017, **28**, 4553–4564.

45 S. B. Amor, A. Benali, M. Bejar, E. Dhahri, K. Khirouni, M. A. Valente, M. P. F. Graça, F. Al-Turjman, J. Rodriguez and A. Radwane, Modulation of magnetism and study of impedance and alternating current conductivity of $Zn_{0.4}Ni_{0.6}Fe_2O_4$ spinel ferrite, *J. Mol. Struct.*, 2019, **1184**, 298–304.

46 U. Hanifah and D. Triyono, *AIP Conference Proceedings, Dielectric properties enhancement of Mg doped $LaFeO_3$ perovskite materials at room temperature*, 2020, vol. 2242, p. 020004.

47 B. Behera, P. Nayak and R. N. P. Choudhary, Structural and electrical properties of $KCa_2Nb_5O_{15}$ ceramics, *Cent. Eur. J. Phys.*, 2008, **6**, 289.

48 B. C. Sutar, R. N. P. Choudhary and P. R. Das, Dielectric and impedance spectroscopy of $Sr(Bi_{0.5}Nb_{0.5})O_3$ ceramics, *Ceram. Int.*, 2014, **40**, 7791–7798.

49 D. Johnson and Z. Plot, *ZView Electrochemical Impedance Software, Version 2.3b*, Scribner Associates Inc., Southern Pines, 2000.

 © 2021 The Author(s). Published by the Royal Society of Chemistry

Open Access Article. Published on 10 November 2021. Downloaded on 12/4/2025 4:48:14 PM.
This article is licensed under a Creative Commons Attribution-NonCommercial 3.0 Unported Licence.

50 A. Benali, M. Bejar, E. Dhahri, M. F. P. Graça and L. C. Costa, Electrical conductivity and ac dielectric properties of $La_{0.8}Ca_{0.2-x}Pb_xFeO_3$ (x = 0.05, 0.10 and 0.15) perovskite com-pounds, *J. Alloys Compd.*, 2015, **653**, 506–512.
51 H. Issaoui, A. Benali, M. Bejar, E. Dhahri, B. F. O. Costa, M. P. F. Graca and M. A. Valente, *RSC Adv.*, 2020, **10**, 16132–16146.
52 R. A. De Souza, J. Fleig, J. Maier, Z. Zhang, W. Sigle and M. Rühle, Electrical resistance of low-angle tilt grain boundaries in acceptor-doped $SrTiO_3$ as a function of misorientation angle, *J. Appl. Phys.*, 2005, **97**, 053502.
53 D. Triyono, S. N. Fitria and U. Hanifah, Dielectric analysis and electrical conduction mechanism of $La_{1-x}Bi_xFeO_3$ ceramics, *RSC Adv.*, 2020, **10**, 18323–18338.
54 O. Polat, M. Coskun, F. M. Coskun, B. Zengin, K. Durmus, Y. Caglar, M. Caglar and A. Turut, *J. Alloys Compd.*, 2019, **787**, 1212–1224.
55 K. Holderna-Natkaniec, M. O. M. Sghaier, P. Ławniczakc, M. Zdanowska-Fraczek, A. Wozniak-Braszak and S. Chaabouni, Electric properties and internal dynamics of the $[C_6H_{18}N_2]$ $SbCl_5$ $[C_6H_{18}N_2]$ Cl_2 in intermediate temperature phase (part II), *Polyhedron*, 2015, **85**, 131–136.
56 A. K. Jonscher, *Dielectric Relaxation in Solids*, Chelsea Dielectric Press, London, 1983, vol. 658.
57 J. S. Kim, Electric Modulus Spectroscopy of Lithium Tetraborate ($Li_2B_4O_7$) Single 660 Crystal, *J. Phys. Soc. Jpn.*, 2001, **70**, 3129–3133.
58 H. Felhi, R. Lahouli, M. Smari, H. Rahmouni, K. Khirouni and E. Dhahri, Study of the structural, electric and dielectric proprieties of $Bi_{1-x}Nd_xMn_2O_5$ ($x = 0$, $x = 0.1$ and $x = 0.2$), *J. Mol. Struct.*, 2019, **1179**, 1–10.
59 A. Shukla and R. N. P. Choudhary, Study of aliovalent modification on dielectric and ac conductivity properties in lead titanate nanoceramics, *J. Mater. Sci.: Mater. Electron.*, 2011, **22**, 1222–1228.
60 R. S. Devan and B. K. Chougule, Effect of composition on coupled electric, magnetic, and dielectric properties of two-phase particulate magnetoelectric composite, *J. Appl. Phys.*, 2007, **101**, 014109.
61 R. P. Mahajan, K. K. Patankar, M. B. Kothale and S. A. Patil, Conductivity, dielectric behavior and magnetoelectric effect in copper ferrite–barium titanate composites, *Bull. Mater. Sci.*, 2000, **23**, 273–279.
62 E. Barsoukov and J. Ross Macdonald, *Impedance Spectroscopy Theory, Experiment and Applications*, Wiley Interscience, New York, 2nd edn, 2005, pp. 14–41.
63 B. N. Parida, S. Behera, P. R. Das, R. Padhee and R. N. P. Choudhary, Structural, dielectric and electrical properties of a new tungsten bronze ferroelectric ceramics, *J. Mater. Sci.: Mater. Electron.*, 2014, **25**, 2618–2626.
64 J. T. Gudmundsson, H. G. Svavarsson, S. Gudjonsson and H. P. Gislason, *Phys. B*, 2003, **340**, 324–328.
65 M. Pollak, On the frequency dependence of conductivity in amorphous solids, *Philos. Mag.*, 1971, **23**, 519–542.
66 S. Mollah, K. K. Som, K. Bose and B. K. Chaudhuri, ac conductivity in $Bi_4Sr_3Ca_3Cu_yO_x$ (y = 0–5) and $Bi_4Sr_3Ca_{3-z}Li_zCu_4O_x$ (z = 0.1–1.0) semiconducting oxide glasses, *J. Appl. Phys.*, 1993, **74**, 931.
67 A. R. Long, Frequency-dependent loss in amorphous semiconductors, *Adv. Phys.*, 1982, **31**, 553–637.